Journal of Magnetism and Magnetic Materials 177–181 (1998) 970–975

ELSEVIER

Journal of magnetism and magnetic materials

Invited paper

Modelling of exchange-spring permanent magnets

T. Schrefl, J. Fidler*

Institute of Applied and Technical Physics, Vienna University of Technology, Wiedner Hauptstraße 8-10, A-1040 Vienna, Austria

Abstract

Micromagnetic modelling using the finite-element method reveals the correlation between the local arrangement of the magnetic moments on a length scale of several nanometers and the magnetic properties of nanocomposite permanent magnets. Theoretical limits for remanence and coercivity are derived for $Nd_2Fe_{14}B/Fe_3B/\alpha$-Fe nanocrystalline permanent magnets. The coercive field shows a maximum at an average grain size of $D = 20$ nm. Intergrain exchange interactions override the magneto-crystalline anisotropy of the $Nd_2Fe_{14}B$ grains for smaller grains, whereas exchange hardening of the soft phases becomes less effective for larger grains. The calculations show a linear trade off of remanence and coercivity as a function of the α-Fe to Fe_3B ratio. The coercive field H_c and the remanence J_r cover the range $(H_c, J_r) = (340$ kA/m, 1.4 T) to (610 kA/m, 1.1 T) for a composite magnet containing 40% $Nd_2Fe_{14}B$, $(60 - x)$% Fe_3B, and x% α-Fe. The numerical integration of the Gilbert equation yields the transient magnetic states during irreversible switching and thus reveal how reversed domains nucleate and expand.

Keywords: Micromagnetic calculation; Nanocrystalline materials; Rare earth permanent magnets; Exchange interactions; Remanence; Coercivity

1. Introduction

Isotropic, nanocrystalline magnets being composed of magnetically hard and soft particles show high remanence and reasonably large coercive field [1–6], provided that both phases are strongly exchange coupled. Generally, isotropic permanent magnets with a remanence ratio $J_r/J_s > 0.5$ are referred as remanence-enhanced materials. Exchange interactions cause the magnetisation within the soft magnetic grains to be arranged parallel to the average direction of the magnetisation in the neighbouring hard magnetic particles [7]. The demagnetisation curve becomes highly reversible, since the magnetisation within the soft phase may rotate out of its preferred direction in zero field without inducing an irreversible switching of the hard magnetic grains [8]. The high amount of soft magnetic phases reduces the coercive field as compared to isotropic, single-phase materials. Nevertheless, a reasonable energy–density product can be obtained in an isotropic magnet with low rare-earth content, if the composition and the microstructure are carefully adjusted to obtain the desired properties [5]. Micromagnetic modelling helps to understand the basic mechanisms that determine the magnetic properties and provides guidelines for the optimisation of the microstructure. The finite-element method provides a reliable technique for the theoretical treatment of magnetisation processes [9, 10], since it is highly flexible concerning material inhomogeneities and arbitrarily shaped, polycrystalline structures.

A theoretical treatment of the exchange-spring behaviour must take into account the magnetic interactions between the grains. McCallum and coworkers [11] reported an enhanced remanence in melt-spun Nd–Fe–B magnets being composed of nanocrystalline homogeneous grains without any additional phases separating the adjacent grains. Hadjipanayis and Gong [12] showed that intergrain exchange interactions qualitatively explains the relation between remanence and coercive field in Nd–Fe–Al–B–Si magnets, applying a molecular-field

* Corresponding author. Tel.: + 43 1 8801 612; fax: + 43 1 5868 814; e-mail: fidler@email.tuwien.ac.at.

0304-8853/98/$19.00
PII S0304-8853(97)00653-7

model which was originally developed by Callen et al. [13] to treat exchange interactions in amorphous ferromagnets. Using a one-dimensional model, Kneller and Hawig [14] estimated the optimum microstructure to consist of hard grains embedded in a magnetically soft matrix with the lateral dimension of both phases about equal to the domain wall width of the hard magnetic phase. Skomski and Coey [15] derived the remanence and the nucleation field of multilayers being composed of magnetically hard and soft layers. Leineweber and Kronmüller [16] presented a rigorous treatment of hysteresis in a $Nd_2Fe_{14}B/\alpha$-Fe/$Nd_2Fe_{14}B$ multilayer system. They derived three different regimes of magnetisation reversal depending on the thickness of the α-Fe layer. Kitajima and coworkers [17] numerically investigated the effects of intergrain exchange in two-phase α-Fe/$Nd_2Fe_{14}B$ magnets using a model-magnet composed of uniformly magnetised cubes. The results indicate a maximum in the energy–density product as a function of the strength of intergrain exchange interactions.

Numerical micromagnetics based on the finite-element method [18–20] enable a quantitative description of the correlation between the microstructure and the magnetic properties. This article gives a short review of the basic micromagnetic and numerical concepts applied in finite-element micromagnetics of bulk permanent magnets. The calculation of the magnetic properties of a composite $Nd_2Fe_{14}B/Fe_3B/\alpha$-Fe system, consisting of 125 polyhedral grains, reveals the leading microstructural features that determine the magnetic properties of exchange-spring permanent magnets. In addition to static micromagnetic modelling based on energy minimisation, the numerical solution of the Gilbert equation of motion shows how reversed domains nucleate and expand. Finally, the influence of damped gyromagnetic precession on magnetisation reversal is discussed.

2. Micromagnetic and numerical background

The minimisation of the total magnetic Gibb's free energy with respect to magnetic polarisation $\boldsymbol{J} = \beta J_s$, subject to the constraint $|\boldsymbol{J}| = J_s$, yields a stable equilibrium state of a ferromagnetic structure [21]. If one neglects surface anisotropy and magnetoelastic effects, the magnetic Gibb's free energy is the sum of the exchange, the magneto-crystalline anisotropy energy, the magnetostatic energy, and the Zeeman energy of the magnetic polarisation in an external field $\boldsymbol{H}_{ext}$

$$E_t = \int \left[A \sum_{i=1}^{3} (\nabla \beta_i)^2 + f_k(\boldsymbol{J}) - \tfrac{1}{2} \boldsymbol{J} \cdot \boldsymbol{H}_d - \boldsymbol{J} \cdot \boldsymbol{H}_{ext} \right] dV, \quad (1)$$

where A is the exchange constant, $\boldsymbol{H}_d$ the demagnetising field, and f_k the energy density associated with uniaxial ($Nd_2Fe_{14}B$), cubic (α-Fe), or in-plane (Fe_3B) magneto-crystalline anisotropy. The subsequent calculation of equilibrium states for decreasing external field gives the demagnetisation curve in static micromagnetic modelling. The variational derivative of the magnetic Gibb's free energy gives the effective field, $\boldsymbol{H}_{eff} = -\delta E_t / \delta \boldsymbol{J}$, which provides the torque acting on the magnetisation. The Gilbert equation [22],

$$\frac{\partial \boldsymbol{J}}{\partial t} = -|\gamma| \boldsymbol{J} \times \boldsymbol{H}_{eff} + \frac{\alpha}{J_s} \boldsymbol{J} \times \frac{\partial \boldsymbol{J}}{\partial t}, \quad (2)$$

describes the physical path the system proceeds towards equilibrium. Here, γ is the gyromagnetic ratio of the free electron spin and α the Gilbert damping constant. The time integration of Eq. (2) assuming a continuously decreasing external field provides the demagnetisation curve in dynamic micromagnetic calculations. Whereas static micromagnetics give equilibrium states before and after magnetisation reversal, dynamic micromagnetics reveal the equilibrium configurations and the transient states during irreversible switching.

Modelling of grain growth yields realistic three-dimensional microstructures. Starting from randomly located seed points, grains grow with constant growth velocity in each direction. Fig. 1 shows a three-dimensional model system consisting of 125 polyhedral grains. The different phases and the anisotropy directions are randomly assigned to the grains, resulting in a realistic phase distribution. Each grain is further subdivided into tetrahedral finite elements, in order to resolve nonuniform magnetic states on a length scale of a few nanometers. On the finite-element mesh, the magnetic polarisation and a magnetic scalar or a vector potential for field calculation [23–25] are approximated by piecewise linear

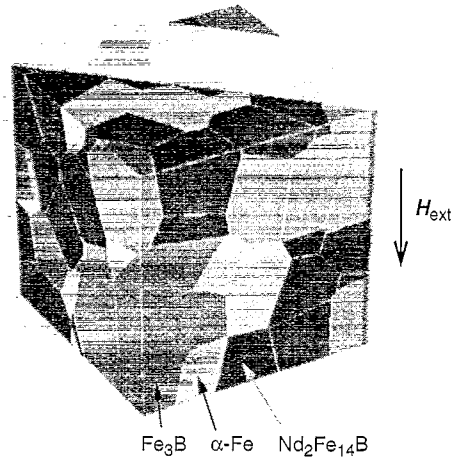

Fig. 1. Finite-element model of a nanocrystalline permanent magnet microstructure composed of 125 polycrystalline grains with the following volume fractions of the phases: 40% $Nd_2Fe_{14}B$, 30% α-Fe, and 30% Fe_3B. The edge length of the cube is varied between 40 and 120 nm. The shaded area gives the slice plane used as probe for plots of the magnetisation.

functions. The use of spherical coordinates to represent $\boldsymbol{J}$ and of a magnetic vector potential to calculate $\boldsymbol{H}_d$ proved to be effective in static micromagnetic calculation [18]. Then the search for an equilibrium state reduces to an unconstrained, algebraic minimisation problem which may be solved by any state-of-the-art minimisation technique [26]. The direction cosines β_i and a magnetic scalar potential are a straightforward choice of the variables in dynamic micromagnetic calculations. The Gilbert equation and Poisson's equation for the scalar potential are discretized by the Galerkin method, leading to a stiff system of algebraic differential equations. Its time integration is performed using backward differentiation formulas with variable step size and variable order [27].

The introduction of a magnetic scalar or vector potential to calculate the demagnetising field eliminates long-range terms from the total magnetic Gibb's free energy and thus reduces computation time and memory requirements. However, the evaluation of the magnetostatic energy using magnetic potentials requires an integration over the entire space outside the magnetic particle. Space transformations or a boundary-element method may be applied, in order to treat this so-called open-boundary problem. The parallelepipedic shell transformation [28] which maps the external space onto a shell surrounding the magnetic particle was applied in static micromagnetic modelling. The numerical integration of the Gilbert equation can be effectively performed using a hybrid finite-element/boundary-element method to evaluate the magnetic scalar potential [29].

3. Results and discussion

Fig. 2 compares the demagnetisation curves obtained from static micromagnetic modelling for different average grain size for a nanocomposite magnet containing 40% $Nd_2Fe_{14}B$, 30% Fe_3B, and 30% α-Fe. The grain structure of Fig. 1 and the intrinsic magnetic properties given in Table 1 were used in the calculations. The solid line denotes the total magnetic polarisation which is the sum of the contribution of $Nd_2Fe_{14}B$ (long dashed line), of Fe_3B (dashed line) and of α-Fe (dotted line). The coercive field shows a maximum at a grain size of about $D = 20$ nm, whereas the remanence increases monotonically with decreasing grain size. Fig. 3 illustrates the grain-size dependence of the remanence. The corresponding isotropic remanence ratio J_r/J_s is 0.81, 0.7, and 0.68 for a grain size of 10, 20, and 30 nm. The smaller the grains, the more uniform is the magnetisation distribution. This mechanism clearly indicates that remanence enhancement in isotropic, nanocomposite magnets has to be attributed to intergrain exchange interactions. With increasing grain size, exchange interactions become less dominant. The magnetisation follows either the

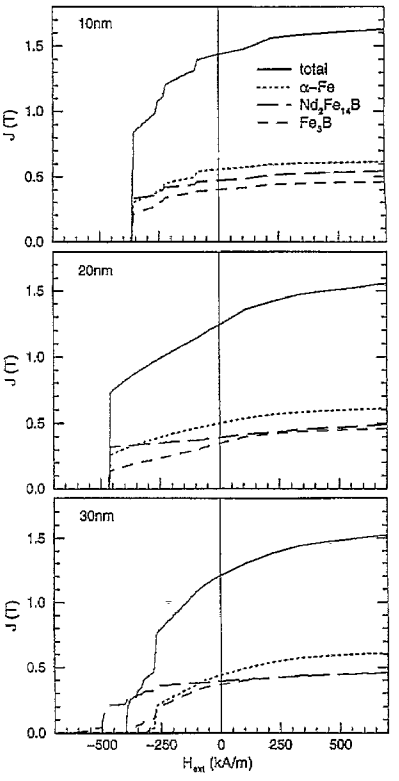

Fig. 2. Influence of grain size on the magnetic properties of the nanocomposite permanent magnet shown in Fig. 1. Demagnetisation curves for a mean grain size of 10, 20, and 30 nm.

Table 1
Intrinsic magnetic properties used for the calculations. J_s (T), spontaneous magnetic polarisation; K_1 and K_2 (MJ/m^3), the anisotropy constants and the exchange constant A (pJ/m)

	J_s	K_1	K_2	A	Reference
$Nd_2Fe_{14}B$	1.61	4.5	0.66	12.5	[30]
Fe_3B	1.62	−0.32		12.5	[31]
α-Fe	2.15	0.046	0.015	25	[32]

magnetocrystalline anisotropy direction within the hard magnetic grains or forms a flux closure structure in soft magnetic regions. Neighbouring Fe_3B or α-Fe grains may make up large continuous areas of soft magnetic phase, where magnetostatic effects will determine the preferred direction of the magnetisation. Within these large soft magnetic regions the magnetisation reverses easily, leading to a decrease of the coercive field for $D \geqslant 20$ nm.

Owing to the competitive effects of magnetocrystalline anisotropy and intergrain exchange interactions, the

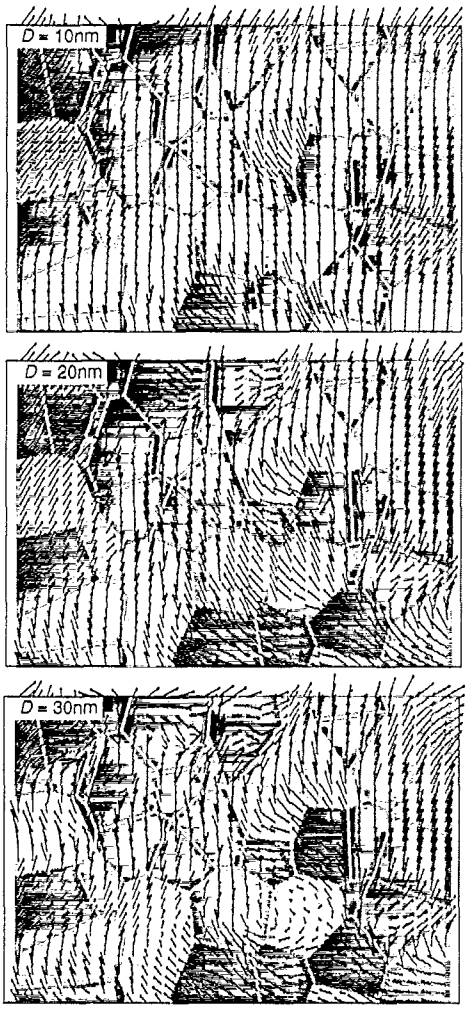

Fig. 3. Magnetisation distribution in a plane parallel to the saturation direction for zero-applied field and a mean grain size of 10, 20, and 30 nm in a composite magnet of 40% $Nd_2Fe_{14}B$, 30% α-Fe, and 30% Fe_3B.

magnetisation of the hard-magnetic grains significantly deviates from the local easy axis for a grain size $D \leqslant$ 20 nm. Fig. 4 shows that the regions, where the magnetisation of the $Nd_2Fe_{14}B$ grains is not parallel to the anisotropy direction, considerably enlarge for decreasing grain size. Regions with an deviation anlge greater than 40° may cover entire hard magnetic grains for $D = 10$ nm. As a consequence coercivity drops, since intergrain-exchange interactions help to overcome the energy barrier for magnetisation reversal. Intergrain exchange and magnetostatic interactions cause the magnetisation to remain correlated during magnetisation reversal. Fig. 5 shows a vortex extending over several grains at an external field of $H_{ext} = -469$ kA/m and $D = 20$ nm.

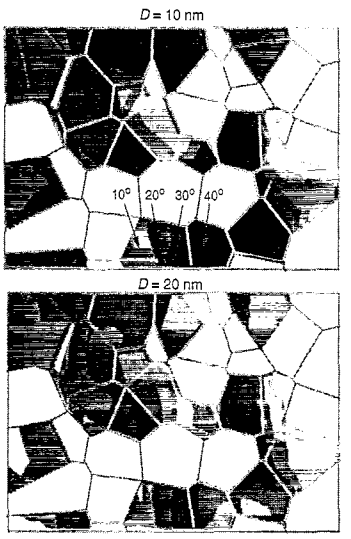

Fig. 4. $Nd_2Fe_{14}B$ grains at zero applied field. The grey scale maps the deviation angle of the magnetisation from the magnetocrystalline anisotropy direction in a plane parallel to the saturation field.

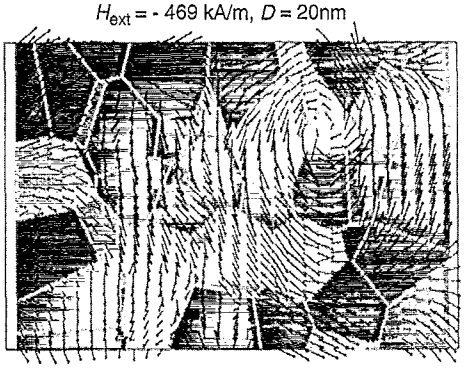

Fig. 5. Magnetisation distribution after irreversible switching in a plane parallel to the saturation direction for an applied field of $H_{ext} = -469$ kA/m and a mean grain size of 20 nm.

Fig. 6 shows the influence of the α-Fe to Fe_3B ratio on demagnetisation curve of a composite magnetic containing 40% $Nd_2Fe_{14}B$ for a mean grain size of 20 nm. Starting from a composite $Nd_2Fe_{14}B$/α-Fe magnet (solid curve), one half of the α-Fe grains are replaced by Fe_3B grains giving a $Nd_2Fe_{14}B/Fe_3B$/α-Fe system (dotted curve). Increasing Fe_3B content improves the coercive field and reduces the remanence. The $Nd_2Fe_{14}B/Fe_3B$ magnet (dashed curve) shows a high coercive field but has a bad loop shape.

Dynamic micromagnetic calculations were performed for a simple microstructure presented in Fig. 7. The model system consists of an α-Fe particle surrounded by 20 $Nd_2Fe_{14}B$ grains. The anisotropy directions of the

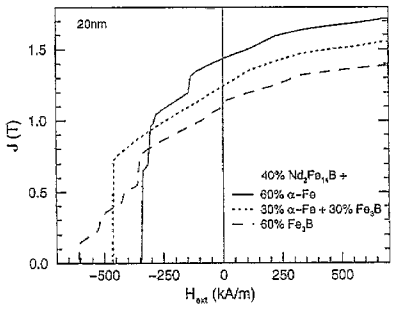

Fig. 6. Influence of the α-Fe to Fe_3B ratio on the magnetic properties of $Nd_2Fe_{14}B$-based composite magnets. Calculated demagnetisation curves for a mean grain size of 20 nm using the grain structure presented in Fig. 1.

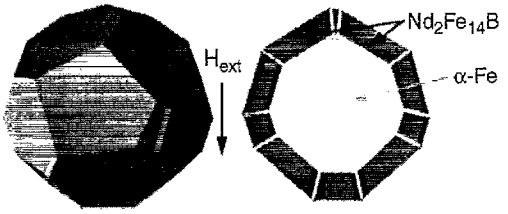

Fig. 7. Model of an exchange-spring magnet used to investigate magnetisation reversal dynamics. Left-hand side: 3D grain structure; right-hand side: slice through the magnet.

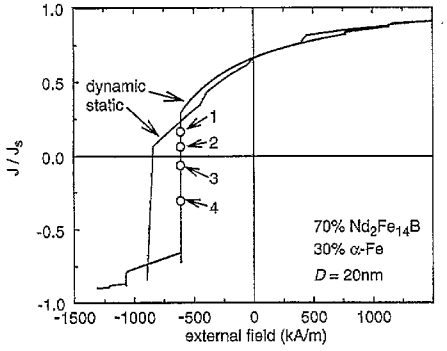

Fig. 8. Demagnetisation curves calculated by energy minimisation (static) and time integration of the Gilbert equation (dynamic) for the model system given in Fig. 7. The numbers refer to the transient magnetic states of Fig. 9.

hard grains were randomly oriented. In order to simplify the calculations, zero magnetocrystalline anisotropy was assumed for α-Fe. The diameter of the α-Fe grain was 20 nm. Fig. 8 compares the demagnetisation curves obtained from static and dynamic micromagnetic calculations with a Gilbert damping constant $\alpha = 0.1$. The gyromagnetic precession taken into account in dynamic micromagnetic calculations causes the system to follow a different path through the energy landscape, leading to a decrease of coercivity with decreasing Gilbert damping constant. A similar dependence of the coercivity on the damping constant was reported in CoPt thin films [33] and in longitudinal magnetic recording media [34]. The magnetisation reversal process is dominated by reversible rotations of the magnetic moments within the soft magnetic grain. The magnetisation of the α-Fe particle remains moderately uniform up to an external field of $H_{ext} = -400$ kA/m. Irreversible switching is caused by the expansion of a vortex-like state which initially forms at the interface between the different phases. Fig. 9 gives transient magnetic states during irreversible switching at $H_{ext} = -611$ kA/m. The reversal of a neighbouring hard magnetic grain starts, when the expense of exchange energy at the interface becomes too large. Thus, the strength of intergranular-exchange interactions will influence the magnetic properties. A thin intergranular phase that reduces the exchange interaction between the different phases shifts the onset of irreversible switching towards higher values of the opposing field and deteriorates the squareness of the demagnetisation curve [8].

Single-phase $Nd_2Fe_{14}B$ magnets and two-phase $Nd_2Fe_{14}B/\alpha$-Fe magnets were modelled in previous papers [19, 20, 35]. The emphasis of this work is the influence of the phase distribution in $Nd_2Fe_{14}B/Fe_3B/\alpha$-Fe composite magnets. The micromagnetic predictions of coercivity and remanence cover the range of $(H_c, J_r) =$ (340 kA/m, 1.4 T) to (610 kA/m, 1.1 T). Fig. 10 shows this upper limit for the magnetic properties in the (H_c, J_r)-plane. Taking into account gyromagnetic precession and nonmagnetic, intergranular phases will shift the line towards lower values of H_c and J_r. The points refer to experimental values [1, 2, 5, 6], which are close to the theoretical predictions.

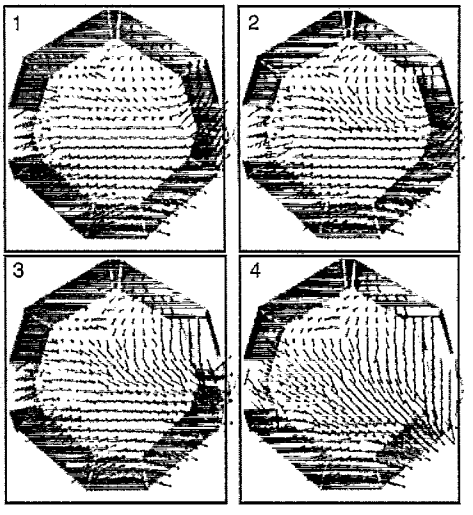

Fig. 9. Nucleation and expansion of reversed domains in an α-Fe/$Nd_2Fe_{14}B$ magnet. The plots give the magnetisation distribution in a slice plane parallel to the external field.

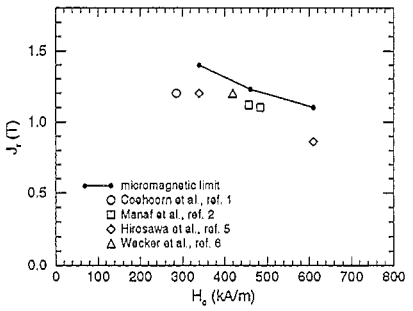

Fig. 10. The relation between coercivity and remanence calculated for 40% $Nd_2Fe_{14}B$ and $D = 20$ nm for varying α-Fe to Fe_3B ratio. The points refer to experimental values [1, 2, 5, 6].

This work has been supported by the Austrian Science Foundation FWF (Grant No. P10511-NAW) and the EC-BRITE/EURAM project BRPR-CT95-0097.

References

[1] R. Coehoorn, D.B. DeMooij, C. DeWaard, J. Magn. Magn. Mater. 80 (1989) 101.
[2] A. Manaf, R.A. Buckley, H.A. Davies, J. Magn. Magn. Mater. 128 (1993) 302.
[3] H.A. Davies, A. Manaf, M. Leonowicz, P.Z. Zhang, S.J. Dobson, R.A. Buckley, Nanostructured Materials, vol. 2, Pergamon, New York, 1993, p. 197.
[4] J. Ding, P.G. McCormik, R. Street, J. Magn. Magn. Mater. 124 (1993) 1.
[5] S. Hirosawa, H. Kanekiyo, Proc. 13th Int. Workshop on RE Magnets and their Application, Birmingham, 1994, p. 87.
[6] J. Wecker, K. Schnitzke, H. Cerva, W. Grogger, Appl. Phys. Lett. 67 (1995) 563.
[7] M.G. Grönefeld, Ph.D. Thesis, University of Stuttgart, Germany, 1990.
[8] T. Schrefl, H. Roitner, J.F. Fidler, J. Appl. Phys. 81 (1997) 5567.
[9] D.R. Fredkin, T.R. Koehler, IEEE Trans. Magn. 23 (1987) 3385.
[10] T. Schrefl, J. Fidler, J. Magn. Magn. Mater. 111 (1992) 105.
[11] R.W. McCallum, A.M. Kadin, G.B. Clemente, J.E. Keem. J. Appl. Phys. 61 (1987) 3577.
[12] G.C. Hadjipanayis, W. Gong, J. Appl. Phys. 64 (1988) 5559.
[13] E. Callen, Y.J. Liu, J.R. Cullen, Phys. Rev. B 16 (1977) 263.
[14] E.F. Kneller, R. Hawig, IEEE Trans. Magn. 27 (1991) 3588.
[15] R. Skomski, J.M.D. Coey, Phys. Rev. B 52 (1993) 15812.
[16] T. Leineweber, H. Kronmüller, Phys. Stat. Sol. (b) 201 (1997) 291.
[17] N. Kitajima, H. Inoue, Y. Kanai, H. Fukunaga, Proc. 3rd Int. Symp. on Physics of Magnetic Materials (ISPMM 95), Seoul, Korea, 1995, p. 652.
[18] T. Schrefl, J. Fidler, H. Kronmüller, Phys. Rev. B 49 (1994) 6100.
[19] T. Schrefl, R. Fischer, J. Fidler, H. Kronmüller, J. Appl. Phys. 76 (1994) 7053.
[20] R. Fischer, T. Schrefl, H. Kronmüller, J. Fidler, J. Magn. Magn. Mater. 150 (1995) 329.
[21] W.F. Brown Jr., Micromagnetics, Wiley, New York, London, 1963.
[22] T. Gilbert, Phys. Rev. 100 (1955) 1243.
[23] P. Asselin, A.A. Thiele, IEEE Trans. Magn. 22 (1986) 1876.
[24] N.A. Demerdash, T.W. Nehl, F.A. Fouad, IEEE Trans. Magn. 16 (1980) 1092.
[25] D.R. Fredkin, T.R. Koehler, IEEE Trans. Magn. 26 (1990) 415.
[26] P.E. Gill, W. Murray, M.H. Wright, Practical Optimization, Academic Press, London, 1981.
[27] A.C. Hindmarsh, L.R. Petzold, Comput. Phys. 9 (1995) 148.
[28] X. Brunotte, G. Meunier, J.C. Sabonnadire, IEEE Trans. Magn. 26 (1990) 588.
[29] T. Schrefl, J. Fidler, K. Kirk, J.N. Chapman, J. Magn. Magn. Mater., in press.
[30] M. Sagawa, S. Fujimura, H. Yamamoto, Y. Mastuura, S. Hirosawa, J. Appl. Phys. 57 (1985) 4094.
[31] W. Coene, F. Hakkens, R. Coehoorn, B.D. de Mooij, C. De Waard, J. Fidler, R. Grössinger, J. Magn. Magn. Mater. 96 (1991) 189.
[32] E. Kneller, Ferromagnetism, Springer, Berlin, 1962.
[33] R.H. Victora, C.F. Brucker, F.E. Spada, J. Magn. Magn. Mater. 97 (1991) 343.
[34] Q. Peng, H.N. Bertram, IEEE Trans. Magn., in press.
[35] R. Fischer, H. Kronmüller, Phys. Rev. B 54 (1996) 7284.